Journal of Sound and Vibration 426 (2018) 54–74

Contents lists available at ScienceDirect

Journal of Sound and Vibration

journal homepage: www.elsevier.com/locate/jsvi

Influence of hole shape on sound absorption of underwater anechoic layers

Changzheng Ye [a, b], Xuewei Liu [a, b], Fengxian Xin [a, b, *], Tian Jian Lu [a, b]

[a] State Key Laboratory for Strength and Vibration of Mechanical Structures, Xi'an Jiaotong University, Xi'an 710049, PR China
[b] MOE Key Laboratory for Multifunctional Materials and Structures, Xi'an Jiaotong University, Xi'an 710049, PR China

ARTICLE INFO

Article history:
Received 8 June 2017
Received in revised form 6 April 2018
Accepted 6 April 2018
Available online 24 April 2018
Handling Editor: R.E. Musafir

Keywords:
Underwater anechoic layer
Sound absorption
Hole shape
Analytical modeling

ABSTRACT

A theoretical model is established to evaluate the sound absorption performance of underwater anechoic layers containing periodically distributed axial holes. Based on the concept for homogenized equivalent layer and on the theory of wave propagation in viscoelastic cylindrical tubes, the transfer function method is used to obtain the absorption coefficient of the anechoic layer adhered on the rigid plate. Three different types of axial holes are considered, the cylindrical, the conical and the horn shaped one. Results obtained with full finite element simulations are used to validate the model predictions. For each hole type, the vibration characteristics of the anechoic layer as well as the propagation of longitudinal and transverse waves in the layer are analyzed in detail to explore the physical mechanisms underlying its absorption performance. Furthermore, a three-dimensional finite element model for oblique incidence is developed to study the effect of hole shape at different incidence angles. The results show that two new absorption peaks appear since the oblique incidence excites two horizontal modes. Among the three hole types, the horn one achieves the best absorption performance at relatively low frequencies both in normal incidence and in oblique incidence.

1. Introduction

Underwater anechoic layer is vital for the acoustic stealth of submarines, which is usually made up of rubber coatings containing periodically distributed inner holes. Early in the 1950s, Blake [1], White [2] and Meyer et al. [3] investigated oscillations and wave propagation in solid media with inner holes. Gaunaurd [4] then established an one-dimensional (1D) model to analyze the eigenfrequency and acoustic absorption of a viscoelastic medium containing short cylindrical holes. Subsequently, Lane [5] and Gaunaurd [6] revealed two types of resonance mechanism for Alberich anechoic layers, i.e., radial motion of hole wall and drum-like oscillation of cover layer, and discussed their relative importance. While Jackins et al. [7] and Strifors et al. [8] studied the reflection of bilaminar structures, Jackins et al. [7] constructed the resonance scattering theory for the reflection of a bilaminar rubber containing spherical air-filled perforations of various concentrations in each layer. Taking the fluid-loaded coated elastic plate into consideration, Strifors et al. [8] analyzed the reflection of a bilaminar structure consisted of a viscoelastic coating and a coated elastic plate. It has been established that the method of transfer function is convenient for calculating the acoustic characteristics of multilayered structures. Cervenka et al. [9] deduced the

* Corresponding author. State Key Laboratory for Strength and Vibration of Mechanical Structures, Xi'an Jiaotong University, Xi'an 710049, PR China.
E-mail addresses: fengxian.xin@gmail.com (F. Xin), tjlu@mail.xjtu.edu.cn (T.J. Lu).

https://doi.org/10.1016/j.jsv.2018.04.008
0022-460X/

transfer matrix of a multilayered structure of which each layer can be either liquid or solid. Stepanishen et al. [10] and Liang et al. [11] studied the acoustic performance of a multilayered structure at oblique incidence, using the transfer function method. As to the anechoic layer with gradually varying axial holes, the concept of equivalent layering needs to be introduced. Tang et al. [12] proposed a two-dimension analytical model for axisymmetric wave propagating in cylindrical tubes, and concluded that only the first effective wave propagation mode needed to be considered at low frequencies. Further, by applying the transfer function method, Tao [13] studied such a kind of anechoic layers containing conical, sinusoidal or cosinoidal holes by layering the gradually varying axial holes into a cluster of cylindrical holes with different diameters so that each layer may be approximated as a cylindrical tube. .

Apart from theoretical analyses, finite element method (FEM) has been employed to study various kinds of anechoic layers. Hennion et al. [14] and Easwaran et al. [15] developed finite element (FE) models to calculate the acoustic properties of anechoic layer containing doubly periodic holes. Langlet et al. [16] further investigated the difference in resonance frequencies between plates without holes and those with holes, while Hennion et al. [17] constructed a FE model for anechoic layer containing grating of elastic tubes. Panigrahi et al. [18] investigated acoustic coatings with different sizes of air channel adhered on the same side or different sides of a steel wall. In addition to FEM, experimentally, Peng et al. [19] developed a modified method to measure the transmission coefficient of a multilayer acoustical panel in impedance tube. They improved the measuring precision and reduced the demand of the tube end.

Although acoustic coatings containing solid particles that may play the role of scattering [20] or local resonance have been proposed [21–24], such coatings are relatively heavy in comparison with those containing inner holes. It is therefore important to investigate the influence of hole shape on acoustic properties of coatings containing inner holes. Ivansson studied anechoic coatings with spherical [25] and superellipsoid [26] holes by adapting techniques used in electron scattering and band-gap computations for photonic and phononic crystals. Ivansson [27] compared anechoic coatings containing cylindrical holes having different cross-sectional shapes (circle, ellipse and superellipse) and used Markov-chain Monte Carlo method to obtain optimal solutions. Shang et al. [28] found that conical holes are superior to cylindrical holes for enhancing the sound absorption performance of anechoic layers. On the other hand, the backing effects [29–31] have been well investigated when the anechoic layer is attached with elastic plates in recent years. However, these works [29–31] still lack detailed analyses for the effect of different inner holes in anechoic layers. In this point, a lot of researches connected to heterogeneous foams for airborne sound [32–34] can provide interesting insights to the present underwater sound, especially for the works regarding with double porosity materials [35–37].

Rubber-based anechoic layers containing gradually varying axial holes are widely used as submarine acoustic coatings. Due to the close impedance between water and rubber as well as the gradually varying impedance of the anechoic layer along its thickness direction, an incident wave can easily propagate into the layer and then be gradually absorbed. Although existing researches [13,28] have examined how various hole shapes, such as cylindrical, conical and horn-like holes, affect the acoustic performance of anechoic layers, further research is needed to explore the profound absorption mechanism of the layer, quantify the absorption difference among various hole shapes, and provide exact equations describing the absorption curve of horn-like holes. To address these issues, the current study employs the transfer function method to establish a theoretical model for analyzing the sound absorption property of anechoic layers containing periodically distributed and gradually varying axial holes; the concept of equivalent layering as well as the existing theory of wave propagation in viscoelastic cylindrical tubes are also employed. For validation, the commercially available FE code COMSOL Multiphysics is used to obtain full numerical results and compare with theoretical model predictions. Three kinds of hole configurations are modeled: the cylindrical hole, the conical, and the horn shaped one, with the exponential function chosen to describe the generatrix of the horn hole. Special focus is placed upon the propagation of longitudinal and transverse waves in the anechoic layer and the effect of hole configuration on sound absorption. To address the oblique incidence case, a three-dimensional FE model is developed to analyze the influence of different hole shapes and different incidence angle on sound absorption performance of the underwater anechoic layer.

2. Theoretical model

In this section, we will develop a theoretical model by combining the two-dimensional simplification approach for axisymmetric wave propagating in cylindrical tube [12] and the layer-wise method for a anechoic layer with gradually varying axial holes [13]. In this model, the homogenization approach is used to calculate the effective acoustic impedance for each divided layer, and then the transfer matrix method is adopted to calculate the sound absorption coefficient.

Fig. 1 presents the configuration and working condition of a representative underwater anechoic layer (rubber) containing periodic inner holes that is adhered to a steel plate. The transverse size of the bi-layer structure is assumed to be infinite. The medium at one side of the structure is water while the medium at the other side is air, both taken as spatially semi-infinite. When an incident plane sound wave propagates from the far field in the water into the anechoic layer, the wave is attenuated. As the steel plate is supposed to be a rigid back, the wave completely reflects back and eventually into the water. For simplicity, only the case of sound waves normal incidence is considered in the theoretical model, while the case of sound wave oblique incidence will be handled by numerical simulations.

A typical arrangement of the periodical holes in the anechoic layer is shown in Fig. 2. In the axial (vertical) direction, the holes keep abreast with each other, while in the transverse (horizontal) direction they conform to regular triangular arrangement. Due to periodicity, only a single cell with hexagonal perimeter needs to be extracted for further study. However,

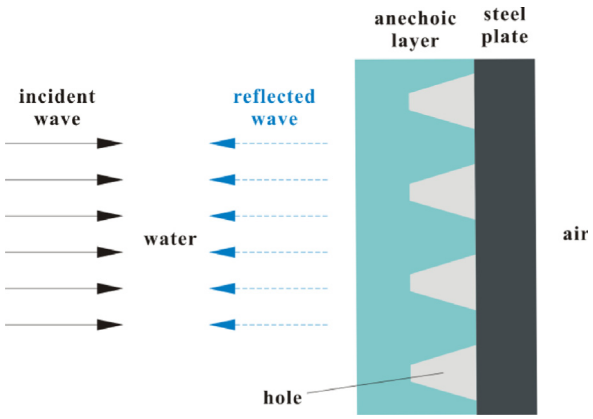

Fig. 1. Configuration and working condition of underwater anechoic layer.

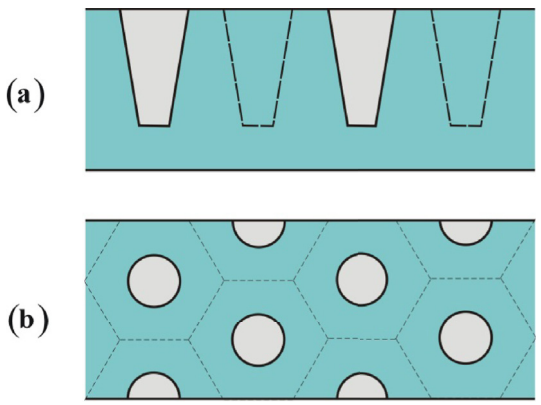

Fig. 2. Typical arrangement of the holes in the anechoic layer: (a) vertical profile; (b) horizontal profile.

the hexagonal cell is difficult to be analyzed theoretically. In the present study, the hexagonal cell is replaced by a cylindrical cell as shown in Fig. 3, that is, with no deformation of the hole, the external shape of the cell is assumed to transform from the original hexagonal one to a cylindrical one. Through such a transformation process, the volume of the cell remains unchanged.

The inner holes of the anechoic layer can have arbitrary shape. In the current study, three representative hope shapes are considered: cylinder, cone and horn. However, for both conical and horn holes, it is difficult to obtain analytical solutions directly. To address this issue, a simplified but approximate approach is employed, as shown schematically in Fig. 4 for the case of conical hole. The axially varying hole is approximated as a cluster of cylindrical holes. The analytical solution thus obtained will be sufficiently accurate as long as the number of segments is large enough. Fig. 5 depicts one such segment, i.e., a cylindrical pipe. Due to axial symmetry, the cylindrical coordinate system rOz is adopted. Let a and b separately denote the inner and outer radii of the pipe, and let l denote its length. Note that, as the axial stress and displacement on the interface

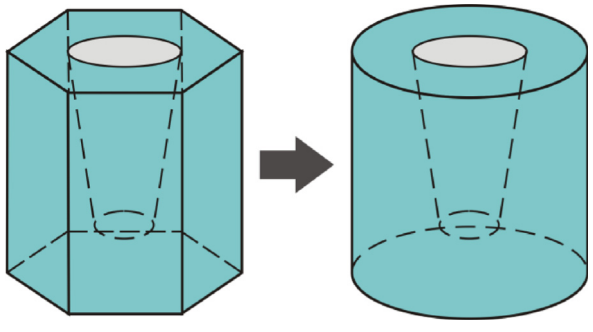

Fig. 3. Simplification of the external shape of a single cell.

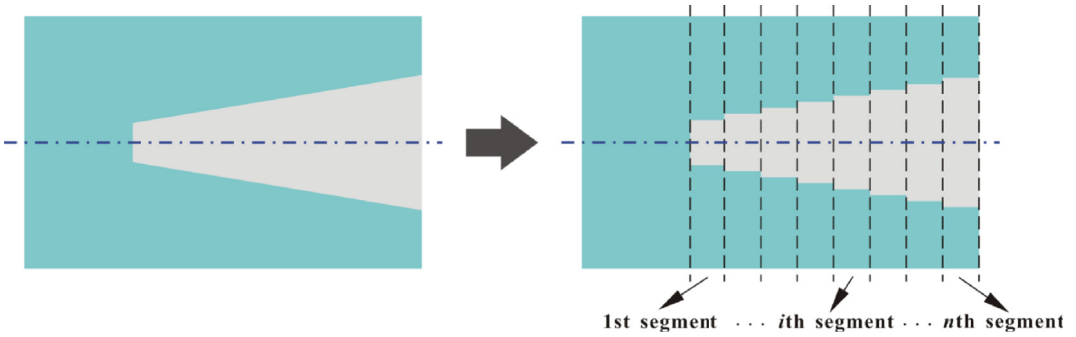

Fig. 4. Conical hole approximated as a cluster of cylindrical holes.

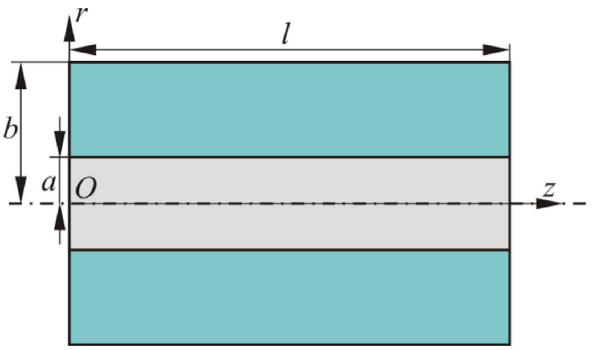

Fig. 5. Profile of acoustic cylindrical pipe model.

between two adjacent cylinder pipes need to be continuous, the origin hole profile should also be smoothly continuous. If a sudden discontinuity in the hole profile exists, this approximation method will not be accurate enough.

The anechoic layer is made up of rubber which is a linear viscoelastic material. For the case of harmonic incident wave, the governing equation can be written as the same form of elastic materials [38]

$$\mu\nabla^2\mathbf{u} + (\lambda+\mu)\nabla(\nabla\cdot\mathbf{u}) = \rho\frac{\partial^2\mathbf{u}}{\partial t^2} \tag{1}$$

where $\mathbf{u}$ is the vector of displacement, t represents time, λ and μ are the Lame constants, ρ is the density of rubber, and ∇ and ∇^2 are the Hamiltonian operator and the Laplace operator, respectively. For a linear viscoelastic material such as rubber, λ and μ are complex numbers while ρ is a real number.

The displacement vector $\mathbf{u}$ can be expressed as [38]

$$\begin{aligned}&\mathbf{u} = \nabla\phi + \nabla\times\boldsymbol{\psi}\\ &\nabla\cdot\boldsymbol{\psi} = 0\end{aligned} \tag{2}$$

where ϕ is a scalar potential function and $\boldsymbol{\psi}$ is a vector potential function. The former is related to longitudinal wave while the latter is related to transverse wave. In consideration of axial symmetry, there is no circumferential component of the transverse wave and so does the second term of $\mathbf{u}$. Because

$$\nabla\times\boldsymbol{\psi} = \frac{1}{r}\left[\frac{\partial\psi_z}{\partial\theta} - \frac{\partial(r\psi_\theta)}{\partial z}\right]\mathbf{e}_r + \left(\frac{\partial\psi_r}{\partial z} - \frac{\partial\psi_z}{\partial r}\right)\mathbf{e}_\theta + \frac{1}{r}\left[\frac{\partial(r\psi_\theta)}{\partial r} - \frac{\partial\psi_r}{\partial\theta}\right]\mathbf{e}_z \tag{3}$$

the radial and axial components of $\boldsymbol{\psi}$ are zero. Consequently, the vector potential function $\boldsymbol{\psi}$ can be degenerated to a scalar potential function ψ, and hence Eq. (2) can be replaced by Helmholtz equations, as:

$$\begin{aligned}&\left(\nabla^2 + k_l^2\right)\phi = 0\\ &\left(\nabla^2 + k_t^2\right)\psi = 0\end{aligned} \tag{4}$$

Here, k_l and k_t are the longitudinal wavenumber and the transverse wavenumber, respectively. $k_l = \omega/c_l$, and $k_t = \omega/c_t$. c_l and c_t denote the speed of longitudinal wave and transverse wave, and ω is the circular frequency.

Solutions of Eq. (4) can be expressed as:

$$\begin{aligned}\phi &= \left[AJ_0(k_{l,r}r) + BY_0(k_{l,r}r)\right]e^{i(k_z z-\omega t)}\\ \psi &= \left[CJ_0(k_{t,r}r) + DY_0(k_{t,r}r)\right]e^{i(k_z z-\omega t)}\end{aligned} \tag{5}$$

where A, B, C and D are coefficients to be determined, $k_{l,r}$ and $k_{t,r}$ are the radial wavenumbers of longitudinal wave and transverse wave, k_z is the axial wavenumber, and $J_0(\cdot)$ and $Y_0(\cdot)$ are the Bessel functions of the first kind and second kind, respectively. The wavenumbers mentioned above are related by:

$$\begin{aligned}k_l^2 &= k_{l,r}^2 + k_z^2\\ k_t^2 &= k_{t,r}^2 + k_z^2\end{aligned} \tag{6}$$

In cylindrical coordinate system, the radial displacement u_r and axial displacement u_z have the following expressions:

$$\begin{aligned}u_r &= \frac{\partial\phi}{\partial r} + \frac{\partial^2\psi}{\partial r\partial z}\\ u_z &= \frac{\partial\phi}{\partial z} - \frac{\partial^2\psi}{\partial r^2} - \frac{\partial\psi}{r\partial r}\end{aligned} \tag{7}$$

In terms of the displacements, the strains are given by:

$$\begin{aligned}\varepsilon_r &= \frac{\partial u_r}{\partial r}\\ \varepsilon_\theta &= \frac{u_r}{r} + \frac{\partial u_\theta}{r\partial\theta}\\ \varepsilon_z &= \frac{\partial u_z}{\partial z}\\ \varepsilon_{rz} &= \frac{\partial u_z}{\partial r} + \frac{\partial u_r}{\partial z}\end{aligned} \tag{8}$$

which are related to the stresses by

$$\begin{aligned}\sigma_r &= \lambda(\varepsilon_r + \varepsilon_\theta + \varepsilon_z) + 2\mu\varepsilon_r\\ \tau_{rz} &= \mu\varepsilon_{rz}\end{aligned} \tag{9}$$

Upon substituting Eq. (7) into Eq. (8) and then into Eq. (9), the relation between the two potential functions, ϕ and ψ, and the two stress components, σ_r and τ_{rz}, can be obtained as:

$$\begin{aligned}\sigma_r &= \lambda\left(\frac{\partial^2\phi}{\partial r^2} + \frac{\partial\phi}{r\partial r} + \frac{\partial^2\phi}{\partial z^2}\right) + 2\mu\left(\frac{\partial^2\phi}{\partial r^2} + \frac{\partial^3\psi}{\partial r^2\partial z}\right)\\ \tau_{rz} &= \mu\left(2\frac{\partial^2\phi}{\partial r\partial z} + \frac{\partial\psi}{r^2\partial r} - \frac{\partial^2\psi}{r\partial r^2} - \frac{\partial^3\psi}{\partial r^3} + \frac{\partial^3\psi}{\partial r\partial z^2}\right)\end{aligned} \tag{10}$$

It is noteworthy that the circumferential displacement u_θ in Eq. (8) is equal to zero as a result of axial symmetry.

After substituting Eq. (5) into Eq. (7) and Eq. (10), the relation between the three variables, u_r, σ_r and τ_{rz}, and the four unknown coefficients, A, B, C and D, can be written as:

$$\begin{Bmatrix}u_r\\ \sigma_r\\ \tau_{rz}\end{Bmatrix} = e^{i(k_z z-\omega t)}\begin{bmatrix}M_{11} & M_{12} & M_{13} & M_{14}\\ M_{21} & M_{22} & M_{23} & M_{24}\\ M_{31} & M_{32} & M_{33} & M_{34}\end{bmatrix}\begin{Bmatrix}A\\ B\\ C\\ D\end{Bmatrix} \tag{11}$$

Expressions of the twelve elements in the above coefficient matrix are given in Appendix A.

Due to periodical arrangement of the holes in the anechoic layer, the interface between two adjacent cells (also the outer boundary of each cell) should comply with the symmetric boundary condition, that is, the normal displacement and shear stress are equal to zero at $r = b$. Besides, since the impedance of air (medium in hole) is far less than that of rubber (matrix

material of anechoic layer), the inner boundary of each cell can be considered as a free interface. In other words, there is no stress at $r = a$, whether it is the normal stress or shear stress. The boundary conditions can thence be written as:

$$\begin{cases} \sigma_r|_{r=a} = 0, & \sigma_{rz}|_{r=a} = 0 \\ u_r|_{r=b} = 0, & \sigma_{rz}|_{r=b} = 0 \end{cases} \tag{12}$$

Substituting Eq. (12) into Eq. (11) leads to the equations for determining the four coefficients A, B, C and D:

$$\begin{bmatrix} M_{11}(b) & M_{12}(b) & M_{13}(b) & M_{14}(b) \\ M_{21}(a) & M_{22}(a) & M_{23}(a) & M_{24}(a) \\ M_{31}(a) & M_{32}(a) & M_{33}(a) & M_{34}(a) \\ M_{31}(b) & M_{32}(b) & M_{33}(b) & M_{34}(b) \end{bmatrix} \begin{Bmatrix} A \\ B \\ C \\ D \end{Bmatrix} = 0 \tag{13}$$

where a and b in the parentheses represent the value of r in each element.

That Eq. (13) has non-zero solution requires the determinant of the coefficient matrix equal to zero:

$$\begin{vmatrix} M_{11}(b) & M_{12}(b) & M_{13}(b) & M_{14}(b) \\ M_{21}(a) & M_{22}(a) & M_{23}(a) & M_{24}(a) \\ M_{31}(a) & M_{32}(a) & M_{33}(a) & M_{34}(a) \\ M_{31}(b) & M_{32}(b) & M_{33}(b) & M_{34}(b) \end{vmatrix} = 0 \tag{14}$$

The solved roots of Eq. (14) are $k_n (n = 1, 2, 3\cdots)$, which are the n-th axisymmetric wavenumbers. It has been proved that in such a cylindrical pipe, the sound absorption performance at low frequencies is mainly influenced by the first axisymmetric wavenumber that associated with the first propagation mode [12,13]. While those wavenumbers of high orders have negligible influences on sound absorption. Therefore, only the first wavenumber k_z is considered and the transfer matrix formulation of Eq. (17) can be used here. If wanting to study the sound absorption performance of cylindrical pipe at high frequencies, more propagation modes (i.e. more wavenumbers) should be required. As such, the transfer matrix formulation of Eq. (17) will be not able to use. In this paper, the low frequency range (i.e. under 10 kHz) is concerned, at which the sound wavelength is far beyond the thickness of the anechoic layer, so that the transfer matrix method is appropriate.

It is noticed that the axial wavenumber of the i th segment is $k_{z,i}$. For convenience of calculation, each segment is considered equivalent to a homogeneous material with corresponding effective parameters. For the i th segment, the effective wavenumber is equal to the axial wavenumber while the effective density is the volumetric average value of rubber density ρ and air density ρ_{air}, namely:

$$\begin{aligned} \tilde{k}_i &= k_{z,i} \\ \tilde{\rho}_i &= \left[1 - \left(\frac{a_i}{b}\right)^2\right]\rho + \left(\frac{a_i}{b}\right)^2 \rho_{\text{air}} \end{aligned} \tag{15}$$

where a_i represents the inner radii of the pipe in the i th layer. The effective impedance of the i th segment is thus given as:

$$\tilde{Z}_i = \tilde{\rho}_i \tilde{c}_i \tag{16}$$

where $\tilde{c}_i = \omega/\tilde{k}_i$ is the corresponding effective sound speed. It is worthy of noting that the homogenization method used here is different from the averaged method used in Ref. [13]. The former gets the acoustic impedance via the effective density and wavenumber of the homogenized segment, while the latter gets the acoustic impedance via the averaged axial stress and displacement at the segment interface. The comparison between the two methods will be shown in the next section, which will demonstrate that the former agrees better with FE simulations over the latter does.

The method of transfer function can be used to relate the two sides of the anechoic layer. Let the interface between the anechoic layer and water medium be the front interface of anechoic layer, and let the interface between the anechoic layer and steel plate as its back interface.

The transfer matrix of the i th segment has the following expression:

$$\mathbf{T}_i = \begin{bmatrix} \cos\left(\tilde{k}_i l_i\right) & -\mathrm{i}\tilde{Z}_i \sin\left(\tilde{k}_i l_i\right) \\ -\dfrac{\mathrm{i}\sin\left(\tilde{k}_i l_i\right)}{\tilde{Z}_i} & \cos\left(\tilde{k}_i l_i\right) \end{bmatrix} \tag{17}$$

where l_i is the thickness of the i th segment. The total transfer matrix of the anechoic layer $\mathbf{T}$ is then the successive multiplication of the transfer matrix of each segment, as:

$$\mathbf{T} = \begin{bmatrix} T_{11} & T_{12} \\ T_{21} & T_{22} \end{bmatrix} = \prod_{i=1}^{n} \mathbf{T}_i \tag{18}$$

In accordance with the transfer function method, the acoustic pressure and vibration velocity of the front interface and the back interface can be related by **T**, as:

$$\begin{Bmatrix} p_f \\ v_f \end{Bmatrix} = \mathbf{T} \begin{Bmatrix} p_b \\ v_b \end{Bmatrix} = \begin{bmatrix} T_{11} & T_{12} \\ T_{21} & T_{22} \end{bmatrix} \begin{Bmatrix} p_b \\ v_b \end{Bmatrix} \tag{19}$$

where p_f and v_f are the acoustic pressure and vibration velocity of the front interface while p_b and v_b are the acoustic pressure and vibration velocity of the back interface, respectively.

The impedance of the front interface Z_f and the back interface Z_b are equal to their corresponding acoustic pressure divided by vibration velocity, as:

$$\begin{aligned} Z_f &= \frac{p_f}{v_f} \\ Z_b &= \frac{p_b}{v_b} \end{aligned} \tag{20}$$

According to Eq. (19) and Eq. (20), one has:

$$Z_f = \frac{T_{11} Z_b + T_{12}}{T_{21} Z_b + T_{22}} \tag{21}$$

Since the steel plate is considered as a rigid back, the impedance of the back interface $Z_b = \infty$, resulting in:

$$Z_f = \frac{T_{11}}{T_{21}} \tag{22}$$

The reflection coefficient of the anechoic layer can be obtained as:

$$R = \frac{Z_f - Z_w}{Z_f + Z_w} \tag{23}$$

where Z_w is the impedance of the water medium.

Finally, due to energy conservation, the sound absorption coefficient α can be calculated as:

$$\alpha = 1 - |R|^2 \tag{24}$$

3. Results and discussion

3.1. Numerical calculation

To validate the present theoretical model, FE simulations are carried out using COMSOL. Due to periodicity, a single cell is simulated using “free triangular” elements, as shown in Fig. 6 for the case of a horn hole. In view of axial symmetry, to simplify the calculation, “space dimension” is set to be “2D axisymmetric”. In the “physics” section, “acoustic-elastic waves interaction” is adopted. The rubber domain is simulated by “elastic waves” component, while the air domain in the hole as well as the external water domain are simulated by “pressure acoustics” component.

As shown in Fig. 7, two typical axial hole shapes, the conical hole and the horn hole, are adopted to calculate and compare with the standard cylindrical hole. In the present study, with focus placed on representative underwater applications, the thickness of the anechoic layer l_a is fixed at 50 mm and the height of hole l_h at 40 mm. The radius of each cell, r_a , is 15 mm. The front and back radii of the hole are denoted as p and q, with the subscript – cylinder, cone or horn – representing the corresponding hole type. The cylindrical coordinate system rOz is also shown in Fig. 7. Both p and q are varied to explore the effects of hole size and hole shape on the sound absorbing capability of the anechoic layer. Correspondingly, displacement and velocity fields in the anechoic layer are compared to reveal the physical mechanisms underlying such effects.

The generatrix of a conical hole is:

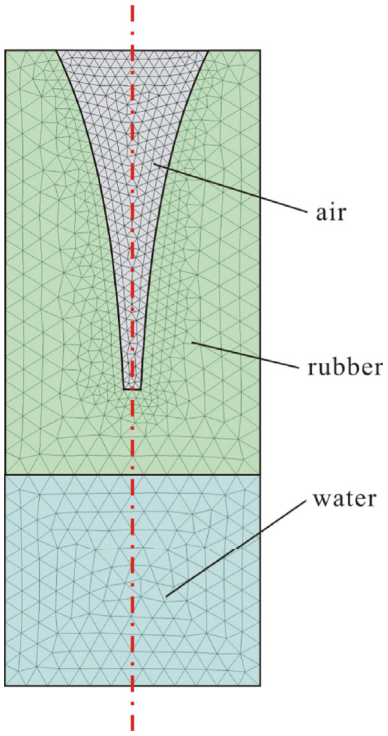

Fig. 6. Mesh in numerical model.

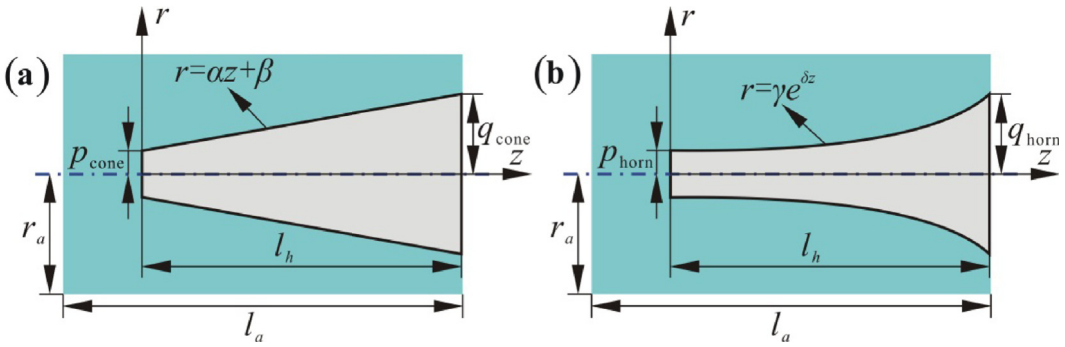

Fig. 7. Parameterized description of the conical (a) and horn (b) holes

$$r = \alpha z + \beta \tag{25}$$

where

$$\alpha = \frac{q_{\text{cone}} - p_{\text{cone}}}{l_h}$$
$$\beta = p_{\text{cone}} \tag{26}$$

The variables in Eq. (25) and Eq. (26) are all quantities with unit of mm, so are those appearing in the following equations of Eq. (27) and Eq. (28).

For the horn hole, exponential function is chosen to describe its generatrix, as:

$$r = \gamma e^{\delta z} \tag{27}$$

where

Table 1
Parameters of material and media.

Parameters	Values
Density of rubber (kg/m^3)	1100
Young's modulus of rubber (GPa)	0.14
Loss factor of rubber	0.23
Poisson ratio of rubber	0.49
Density of air (kg/m^3)	1.21
Density of water (kg/m^3)	998
Sound speed of water (m/s)	1483

$$\gamma = p_{\text{horn}}$$
$$\delta = \frac{1}{l_h}\ln\frac{q_{\text{horn}}}{p_{\text{horn}}} \tag{28}$$

Thus, once p_{cone}, q_{cone} or p_{horn}, q_{horn} are given, the hole shape is determined.

The anechoic layer made of rubber is attached to a steel plate which is considered as a rigid back, as the stiffness of steel is much larger than that of rubber. While air occupies the hole, water is the medium outside the anechoic layer. Table 1 lists the relevant properties of rubber, air and water.

3.2. Effect of hole size on sound absorption

Conical and horn holes having different sizes are investigated to quantify the influence of hole size on sound absorption of anechoic layer. The results of the homogenization method here and the averaged method in Ref. [13] are separately presented

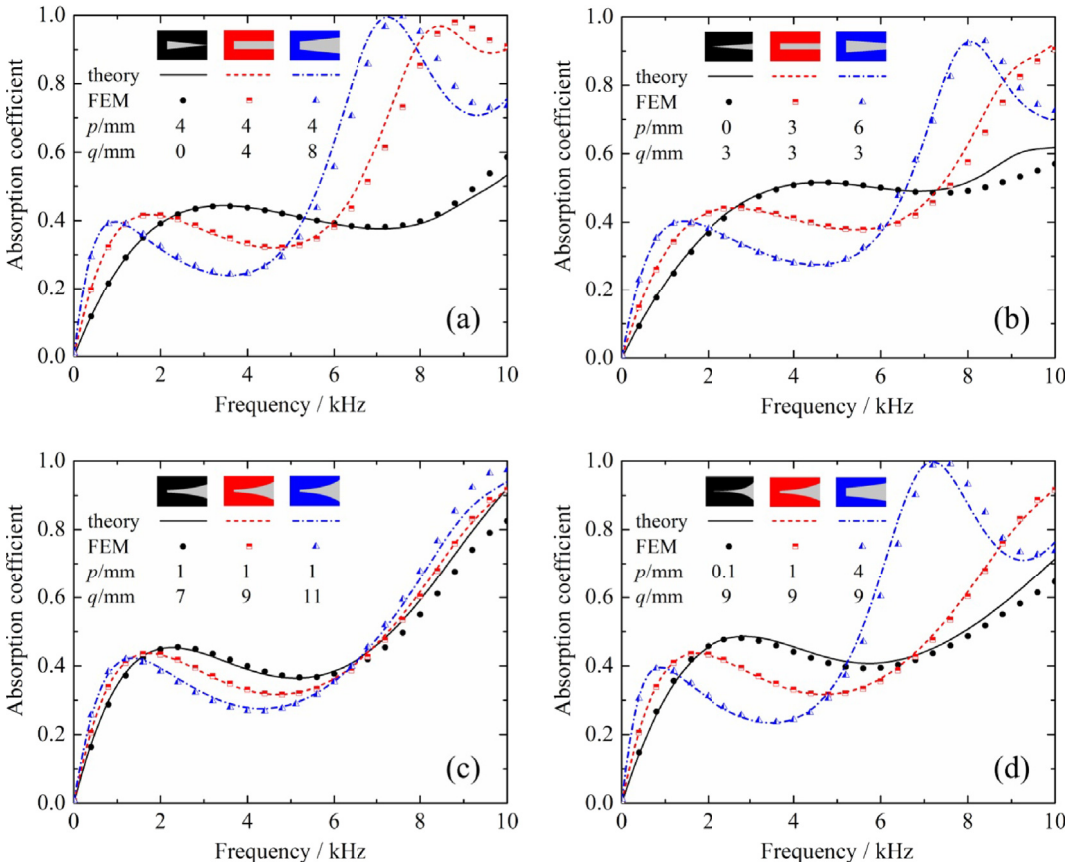

Fig. 8. Comparison between the predictions of the homogenization method and FEM: Sound absorption coefficient of anechoic layer plotted as a function of frequency for selected hole sizes: (a) conical holes with different q_{cone}; (b) conical holes with different p_{cone}; (c) horn holes with different q_{horn}; (d) horn holes with different p_{horn}.

in Fig. 8 and Fig. 9 in terms of absorption coefficient plotted as a function of frequency. In the two figures, (a) and (b) are for conical holes with different q_{cone} and p_{cone}, (c) and (d) stand for horn holes with different q_{horn} and p_{horn}, respectively.

First of all, the results of Fig. 8 demonstrate good consistency between theoretical model predictions and FE simulation results for both conical and horn holes, while the results in Fig. 9 always have relatively larger errors over the considered frequency range. This demonstrates that the homogenization method proposed here is more accurate than the averaged method proposed in Ref. [13]. Therefore, the homogenization method will be employed in the following calculations.

As observed in Fig. 8, with p or q increasing (i.e., the hole becomes bigger), all the absorption curves move towards low frequencies. Each curve exhibits a relatively small crest at low frequency, ensued by a trough at middle frequency, and then a relatively large crest at high frequency. To reveal the mechanism underlying this tendency, corresponding displacement and velocity contours are displayed in Figs. 10 and 11. For illustration, cylindrical hole with $p_{cylinder} = q_{cylinder} = 4$ mm is considered. As the sound wave is normally incident, for cylindrical hole, the longitudinal wave and transverse wave are independent of the axial direction and the radial direction, respectively. In contrast, for conical and horn holes, the two waves are coupling with each other along axial and the radial directions. Thus, the cylindrical hole is employed to better reveal the impact of longitudinal and transverse waves. For the hole considered here, the first crest appears at 1.8 kHz, the first trough at 4.7 kHz and the second crest at 8.8 kHz. Note that, unit simulation is adopted, that is, the initial incidence sound pressure is 1 Pa in FE simulations. In Figs. 10 and 11, the sound incidence wave propagates from the bottom (water domain) of each cell while the top cell surface is fixed on steel plate.

From Fig. 10, it is seen that the three displacements (axial displacement, radial displacement and total displacement) at 4.7 kHz are all much less, in absolute values, than those at the other two frequencies, which persuasively explain why the trough exists at 4.7 kHz. As the displacements at 4.7 kHz are approximately one order smaller than those at the other two frequencies, the displacement contour exhibits almost the same color. Therefore, a group of contours within a narrow scale range are added to the figure to display the distribution of displacement at this frequency.

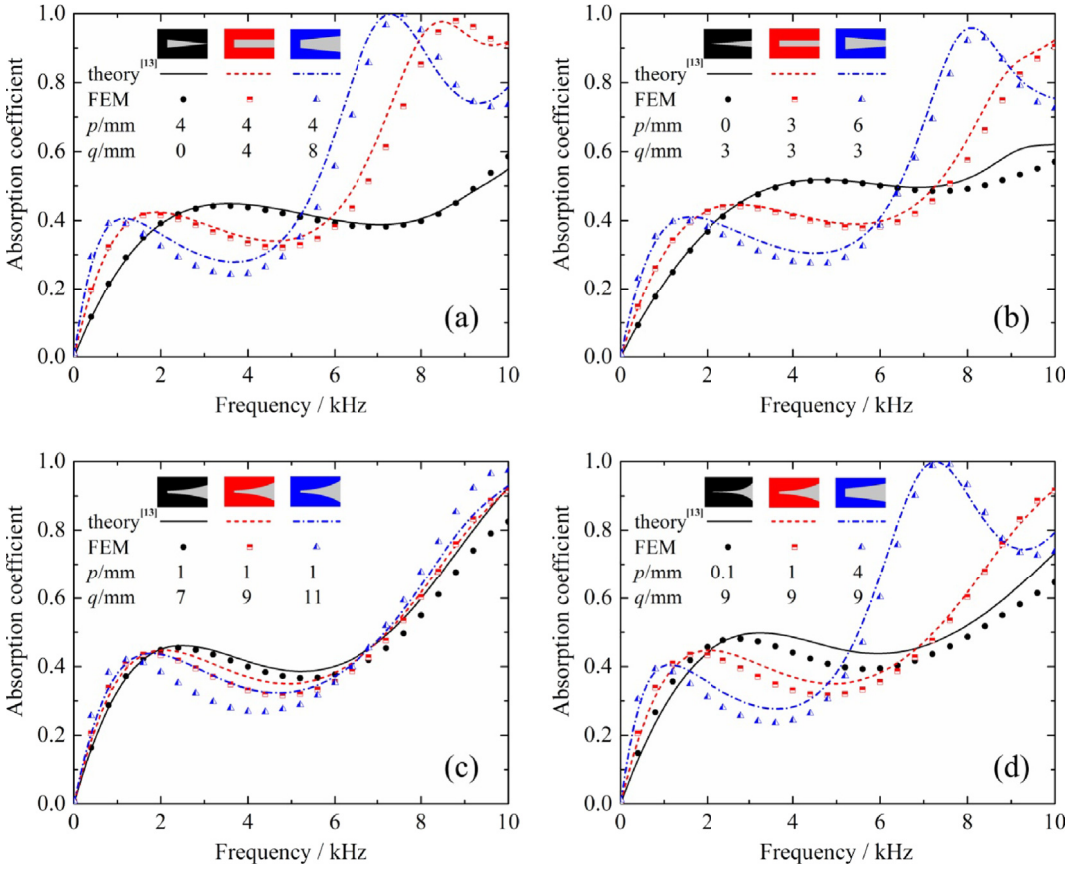

Fig. 9. Comparison between the predictions of the averaged method in Ref. [13] and FEM: Sound absorption coefficient of anechoic layer plotted as a function of frequency for selected hole sizes: (a) conical holes with different q_{cone}; (b) conical holes with different p_{cone}; (c) horn holes with different q_{horn}; (d) horn holes with different p_{horn}.

Next, the two crests are compared with each other. The axial displacement is positive within the whole rubber region at 1.8 kHz, but negative in most of the region at 8.8 kHz, and generally, its absolute value at 1.8 kHz is higher than that at 8.8 kHz. Next, the radial displacement is all negative at 1.8 kHz, while at 8.8 kHz, there is a negative region in the front and a positive region in the back. This may be mainly attributed to the fact that the wave length at high frequencies is shorter than that at low frequencies. Additionally, the absolute value of radial displacement at 8.8 kHz is higher than that at 1.8 kHz, suggesting that the amplitude of transverse wave is greater at high frequencies. Finally, since the radial displacement is smaller than the axial displacement in absolute value, the total displacement is mainly contributed by the latter. As a result, at 1.8 kHz, in the front there exists a region of relatively large total displacement.

The velocity contour is shown in Fig. 11. First of all, it is apparent that the velocities at 1.8 kHz are the smallest. Nevertheless, from Fig. 10, the displacements at this frequency are the largest. Together, they lead to a crest with relatively low value in the absorption curve of Fig. 8(a).

Additionally, apart from the radial velocity, the axial and total velocities at 4.7 kHz have relatively larger regions with high value than those at 8.8 kHz. Instead, the displacement at 4.7 kHz is so small that the advantage from velocity can hardly compensate for the disadvantage from displacement. As a consequence, a trough is formed at 4.7 kHz.

At 8.8 kHz, the absolute value of radial velocity is much larger than that at the other two frequencies. Similar to the case of radial displacement, there is a high value negative region in the front and a high value positive region in the back. Both the radial displacement and radial velocity reflect the propagation of transverse wave. Since, in a viscoelastic medium like rubber, the dissipation to acoustic energy via transverse wave is much stronger than that via longitudinal wave, it is not surprising that the crest with a high value, almost up to 1, exists at 8.8 kHz.

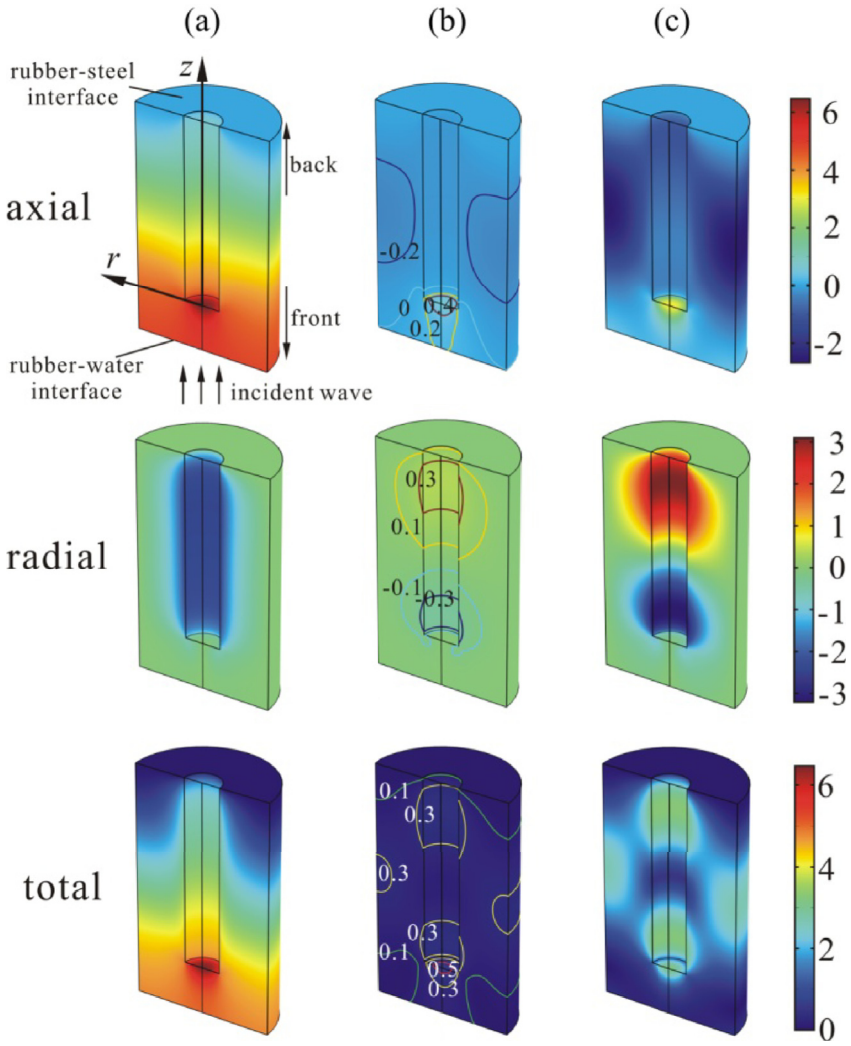

Fig. 10. Displacement contours (axial, radial and total) in rubber domain for a cylindrical hole with $p_{\text{cylinder}} = q_{\text{cylinder}} = 4$ mm (unit: 10^{-11} m) at: (a) 1.8 kHz; (b) 4.7 kHz; (c) 8.8 kHz.

3.3. Comparisons among different hole shapes

In this section, to investigate the influence of hole shape on sound absorption, the volume of the three holes – horn, cone and cylinder – is fixed. From the results shown in Fig. 12, it is seen that while all three holes peak at about 3.6 kHz, the horn hole has the best absorption performance and the cylindrical hole performs the worst. Overall, the horn hole outperforms the other two holes in the broad range from 2 kHz to 8 kHz.

To explore why the horn hole is better than the others, Figs. 13 and 14 compare the displacement and velocity contours in the rubber domain at 3.6 kHz. In the simulation, the initial incidence sound pressure is 1 Pa. In Figs. 13 and 14, the direction of wave propagation is the same as Figs. 10 and 11.

Details of the displacement field are displayed in Fig. 13 for each type of hole. Generally, the three holes exhibit similar trend: the axial displacement decreases along positive axial direction, while the radial displacement negatively increases along negative radial direction. Since the radial displacement is less than the axial displacement, the total displacement has a distribution analogous to that of the axial displacement.

Consider next the axial displacement in more detail. On the one hand, compared with the other two holes, horn hole has a relatively high value region at the horn mouth. On the other hand, cylindrical hole has a highest value region at the front end face. Generally speaking, in the back area, the horn hole has the biggest value region, while the cylindrical hole has the smallest one; in the front area, however, the cylindrical hole has the highest value, while the horn hole has the lowest one.

In comparison, the radial displacement is negative in the whole region, which means its direction is towards the axis. Apart from the vicinity of the hole, the radial displacement is approximately zero everywhere. The closer it is to the hole, the

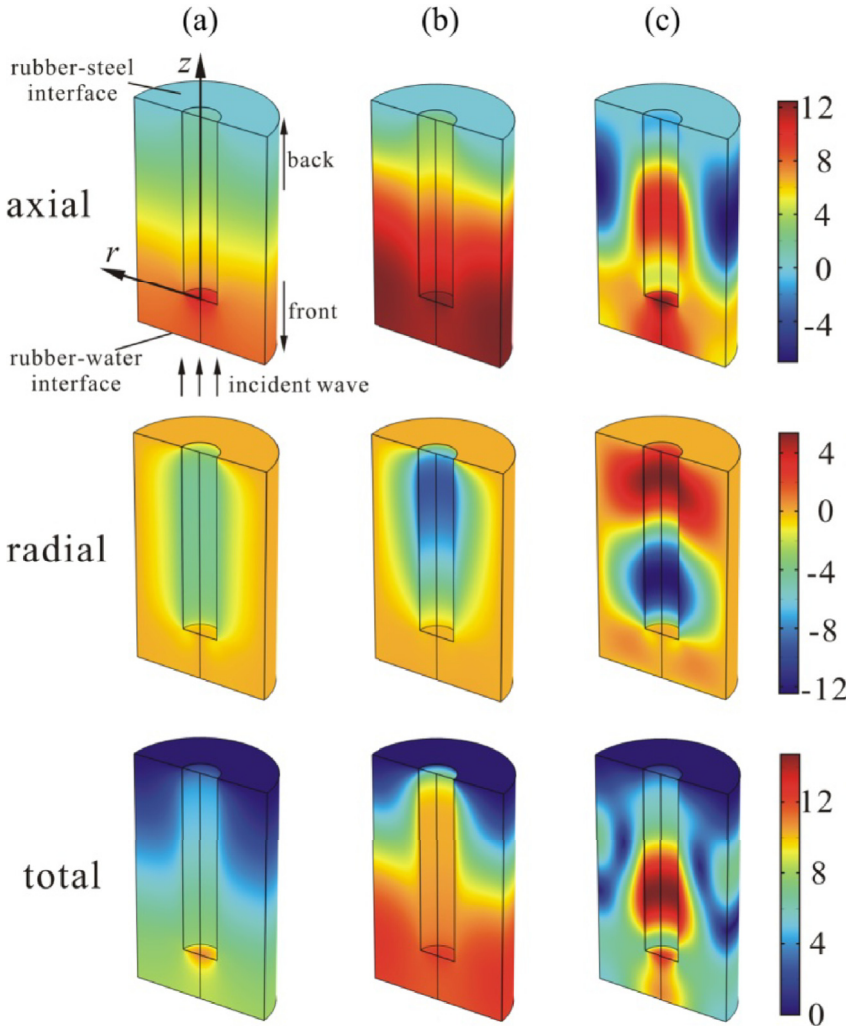

Fig. 11. Velocity contours (axial, radial and total) in rubber domain for a cylindrical hole with $p_{\text{cylinder}} = q_{\text{cylinder}} = 4$ mm (unit: 10^{-7} m/s) at: (a) 1.8 kHz; (b) 4.7 kHz; (c) 8.8 kHz.

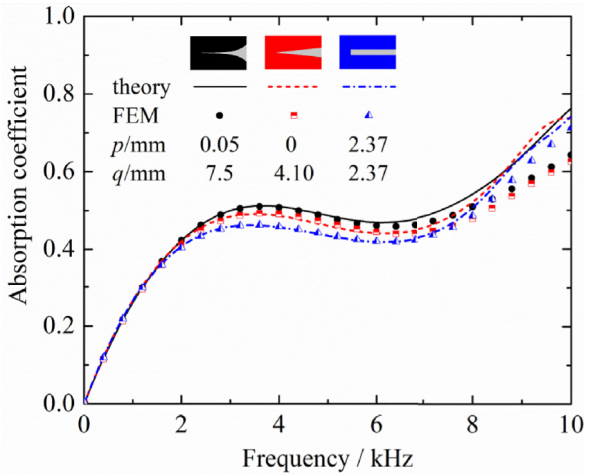

Fig. 12. Sound absorption coefficient versus frequency curves of anechoic layers containing horn, conical and cylindrical holes having the same volume.

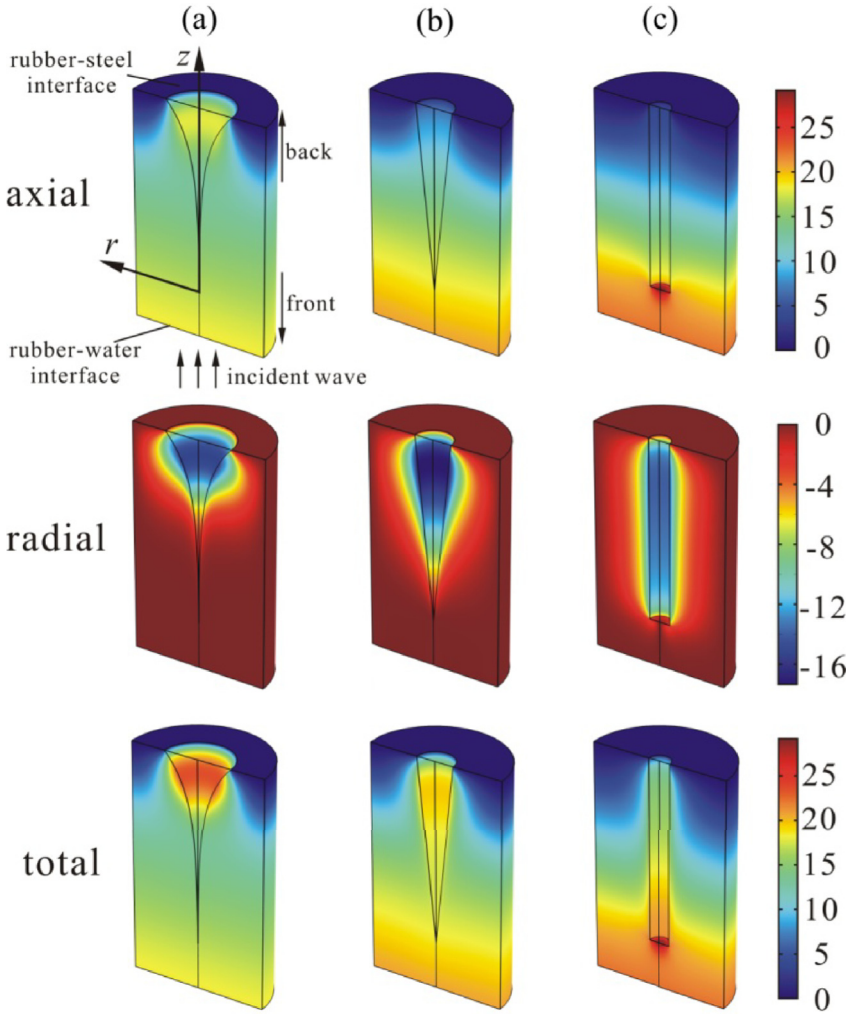

Fig. 13. Comparison of displacement contours (axial, radial and total) in rubber domain at 3.6 kHz (unit: 10^{-12} m) for the: (a) horn hole; (b) conical hole; (c) cylindrical hole.

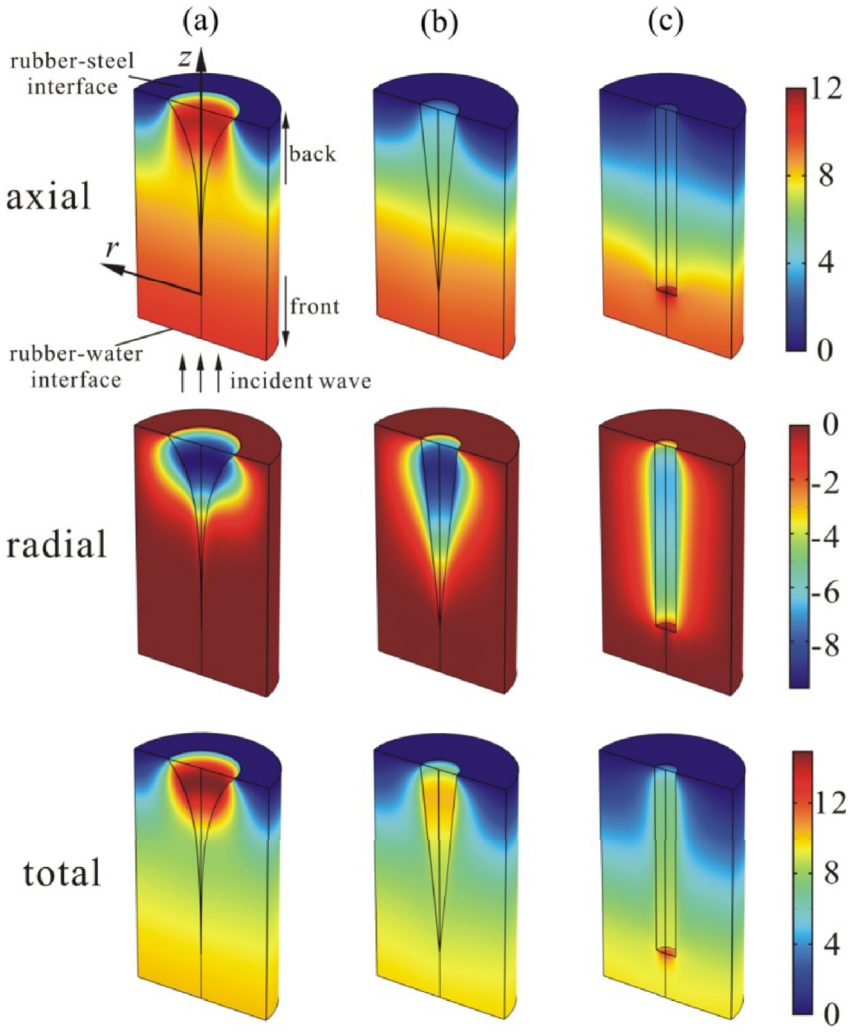

Fig. 14. Comparison of velocity contours (axial, radial and total) in rubber domain at 3.6 kHz (unit: 10^{-7} m/s) for the: (a) horn hole; (b) conical hole; (c) cylindrical hole.

greater the negative value of the radial displacement is. Among the three holes, the conical hole has the highest value in the vicinity of its side face.

The total displacement is the sum of axial and radial displacements. Therefore, in terms of total displacement, the three holes have advantages in different regions: horn mouth for horn hole, side face for conical hole, and front end face for cylindrical hole. It is therefore necessary to examine the corresponding velocity contours to determine which hole type has the superiority.

Fig. 14 compares the velocity fields. For each type of hole, the velocity field has several significant differences from the corresponding displacement field of Fig. 13. Firstly, for horn hole, the axial velocity achieves a high level in most of the rubber domain, especially at the horn mouth. In particular, the high value region is much bigger than that of the other two holes. Secondly, different from the case of radial displacement, the horn hole has the greatest radial velocity near its side face. As a result, the total velocity of the horn hole is greater than that of conical and cylindrical holes in most of the rubber domain, especially at the horn mouth. As the velocity represents the rate of energy dissipation due to vibration, the velocity fields shown in Fig. 14 demonstrate further that the horn hole has superiority in sound absorption.

The results of Figs. 13 and 14 also reveal that the geometric shape of horn hole leads to its advantage in vibration. On one hand, the existence of horn mouth generates an area with great axial vibration in the back of the anechoic layer where the axial vibration is otherwise tiny, and enlarges the area of radial vibration in the back of the anechoic layer due to relatively large hole size relative to the other two holes. On the other hand, the vimineous part in the front of the horn hole expands the area of relatively large axial vibration in the middle and front of the anechoic layer. As a result, the horn hole has the best absorption performance at relatively low frequencies.

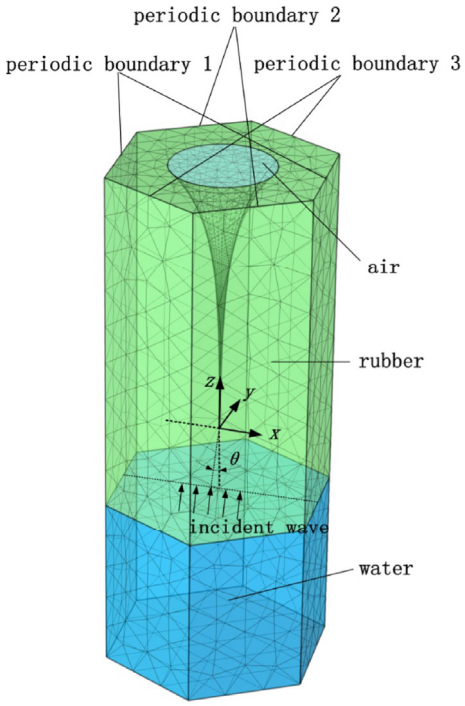

Fig. 15. A three-dimensional FE model for sound oblique incidence.

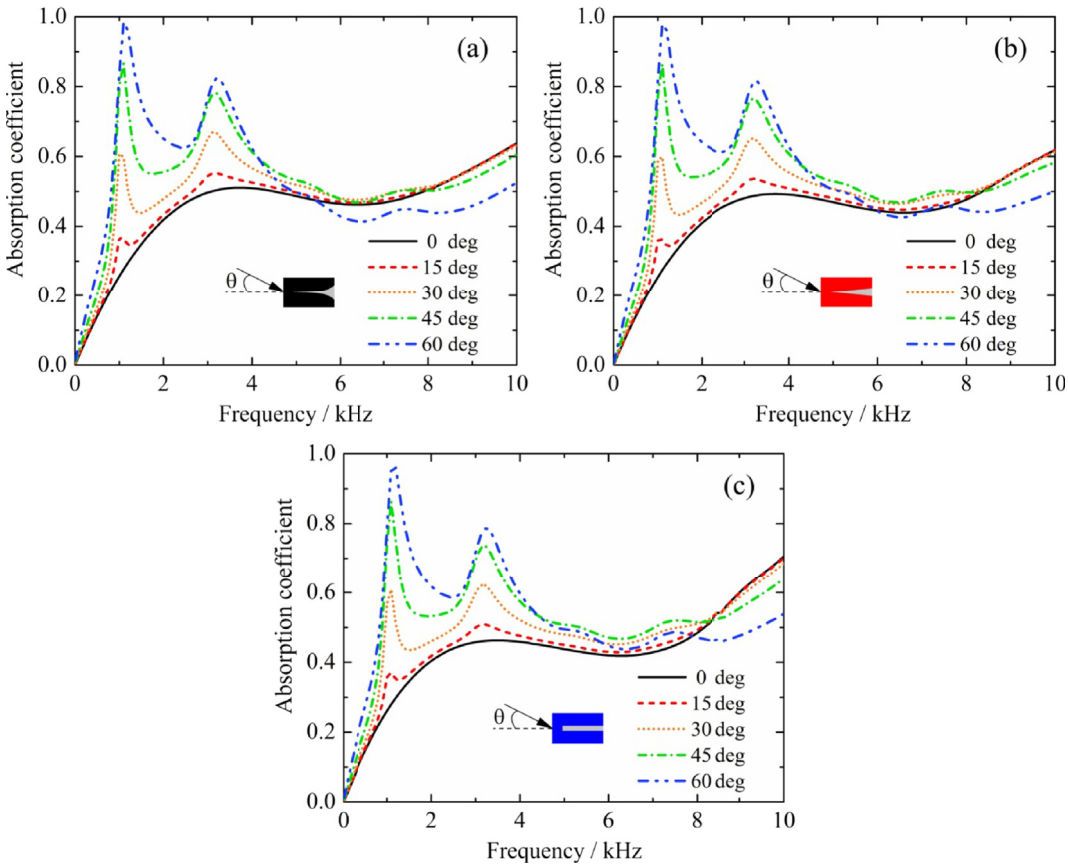

Fig. 16. Influences of incidence angles on sound absorption performance for different hole shapes: (a) horn hole; (b) conical hole; (c) cylindrical hole.

3.4. Oblique incidence simulations and results

As the real situation is not always normal incidence, a three-dimensional FE model is developed to handle with the oblique incidence case in this section. Different from the normal incidence into the anechoic layer, the oblique incidence of sound wave generates non-axisymmetric waves propagating in the layer. In such case, the symmetry boundary condition of Eq. (12) is no more suitable, the normal displacement and shear stress are not equal to zero at $r = b$. So the previous two-dimensional analytical model will not be appropriate for the oblique incidence situation. Considering the difficulties of theoretically solving such a three-dimensional problem, only FE simulations are conducted to study the oblique incidence case in this section.

The three-dimensional FE model is developed by using COMSOL software. As a typical example, a horn hole case with free tetrahedral elements is shown in Fig. 15. The hexagonal cell replaces the previous cylindrical one with an equal volume, and three Floquet periodical conditions are applied on each pair of parallel faces. The incident wave is parallel to the *xz* plane, and impinges on the rubber at an angle θ with the z -axis.

The sound absorption coefficient results for oblique incidence are shown in Figs. 16 and 17. Fig. 16 shows the influences of incidence angles on sound absorption performance at different hole shapes, while Fig. 17 shows the influences of hole shapes on sound absorption performance at different incidence angles. For getting more details, Figs. 18–21 present the longitudinal section deformations and velocity distributions of different hole shape cells at different angles in the rubber domain at the two peak frequencies 1.1 kHz and 3.2 kHz. The longitudinal section is in the *xz* plane and in parallel with the incident wave. In Figs. 18 and 20, the color denotes the value of the total displacement, and the deformations in each figure are magnified in the same value to ensure the comparability among different cases. For simplification, the color denotes the value of the total velocity, and the deformations are magnified in the same value to denote the velocity size and direction in Figs. 19 and 21.

In Fig. 16, comparing with the normal incidence, two obvious new absorption peaks appear in the oblique incidence situations, respectively at 1.1 kHz and 3.2 kHz in all three kinds of hole shapes, and the two peaks become higher with the incidence angles increasing. In reality, the two new peak frequencies correspond to two global horizontal modes of the hexagonal cell, as shown in Figs. 18 and 20, respectively. The two global horizontal modes are just like the two lowest lateral vibration modes of a cantilever beam, though the aspect ratio of the longitudinal section is not large enough and the left and right boundary sides are not free but periodical. In the cases of normal incidence, radial deformation and velocity are mainly

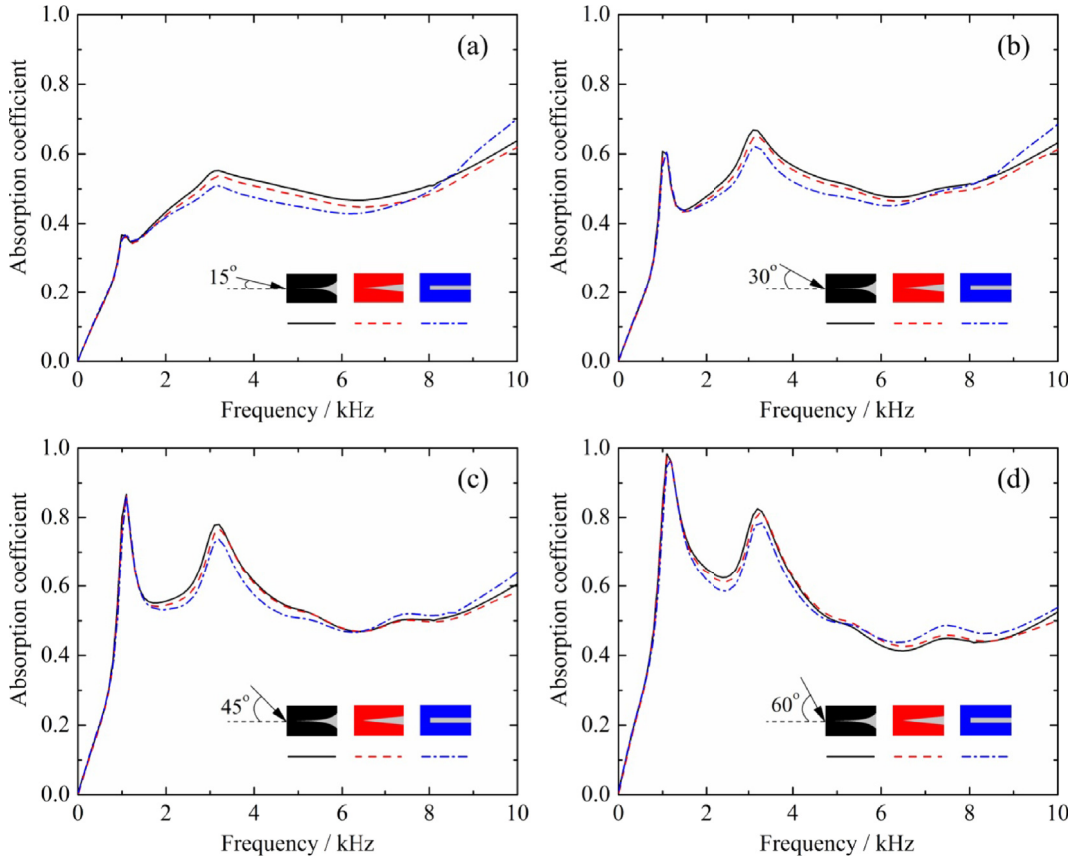

Fig. 17. Influences of hole shapes on sound absorption performance at different incidence angles: (a) 15 deg; (b) 30 deg; (c) 45 deg; (d) 60 deg.

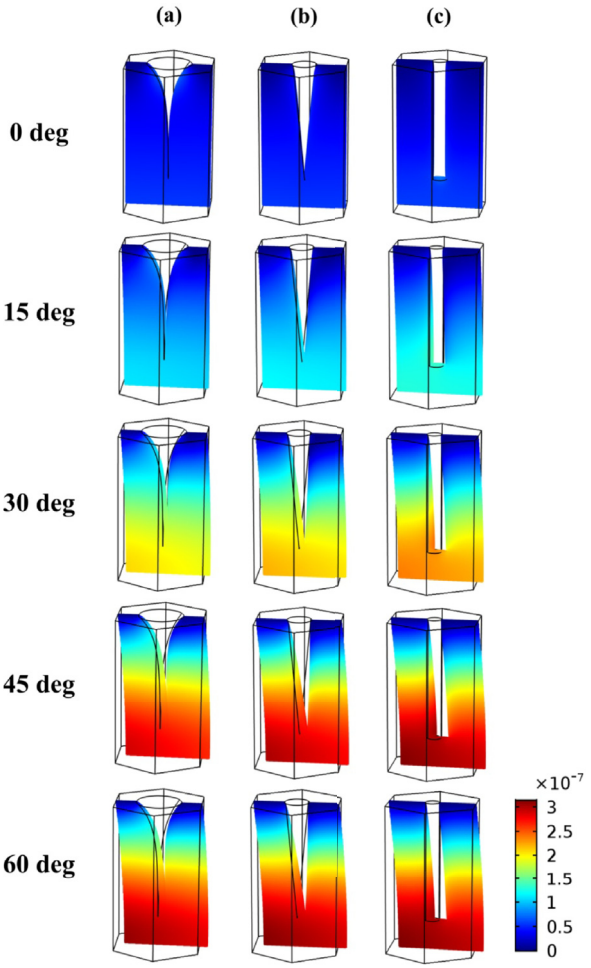

Fig. 18. Comparison of displacements in rubber domain at 1.1 kHz (unit:m) at different incidence angles for the: (a) horn hole; (b) conical hole; (c) cylindrical hole. The color denotes the value of the total displacement.

centered near the holes, as shown in Figs. 13 and 14, i.e. the global horizontal modes cannot be excited by normal incidence. As to the oblique incidence, the global horizontal modes can be excited. With the incidence angle increasing, the horizontal component becomes larger, which can be demonstrated by the deformation and velocity distributions presented in Figs. 18–21. The increase of horizontal component causes more energy dissipation and higher sound absorption coefficient.

Indeed, the increased oblique incidence angle enlarges the propagation distance in rubber and excites the global horizontal modes, which cause larger sound absorption coefficient at relatively low frequencies. While it also increases the reflection coefficient on the water-rubber interface, which causes the sound absorption coefficient decreases at relatively high frequencies. This is obvious for the cases of 45 deg and 60 deg for all three kinds of hole shapes, as shown in Fig. 16.

Another interesting result is that, for each shape hole in Fig. 16, the first absorption peak rises faster than the second peak with the incidence angle increasing. In the case of 15 deg oblique incidence, the fist peak is obviously lower than the second peak, while in the 60 deg case, the first peak is almost 1 and higher than the second peak. This phenomenon is due to the fact that the second peak frequency 3.2 kHz of oblique incidence cases is close to the first peak frequency 3.6 kHz of normal incidence cases. In Figs. 20 and 21, the part near the hole contributes much deformation and velocity, which is similar in Figs. 13 and 14, and hardly seen in Figs. 18 and 19. In Figs. 18 and 19, the deformation and velocity of the first mode gradually increases towards the front face, i.e. the energy dissipation depends mainly on the part near the front end. As the incidence angle increasing, the deformation and velocity of this part rise faster than that of the second mode, and finally the first peak exceeds the second peak in the cases of 45 deg and 60 deg.

In Fig. 17, the influences of hole shapes on the sound absorption performance at different incidence angles are compared. For each angle, the sound absorption performance of horn shape is always better than the other two shapes at relatively low frequencies and the cylindrical hole is worst, which is the same as the normal incidence situation, as shown in Fig. 12. It implies that, in the oblique incidence situation, at relatively low frequencies, the sound absorption mechanism can be classified into two kinds: global vibration dissipation and local vibration dissipation. For global vibration dissipation, the

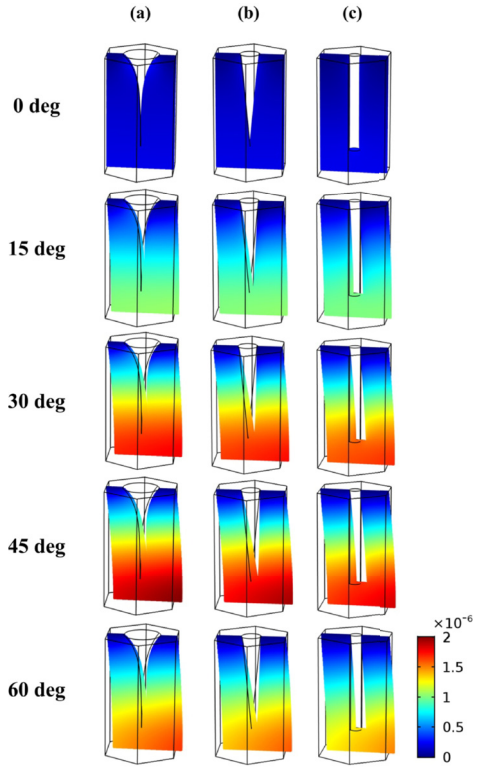

Fig. 19. Comparison of velocities in rubber domain at 1.1 kHz (unit:m/s) at different incidence angles for the: (a) horn hole; (b) conical hole; (c) cylindrical hole. The color denotes the value of the total velocity, and the deformations are magnified in the same value to denote the velocity size and direction.

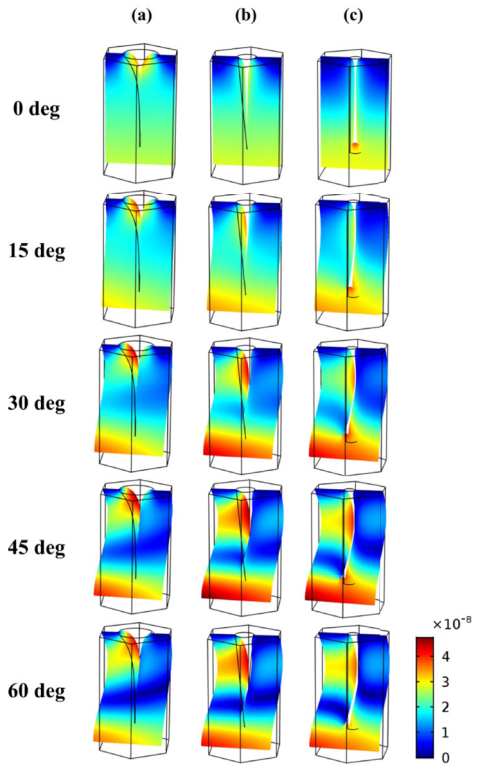

Fig. 20. Comparison of displacements in rubber domain at 3.2 kHz (unit:m) at different incidence angles for the: (a) horn hole; (b) conical hole; (c) cylindrical hole. The color denotes the value of the total displacement.

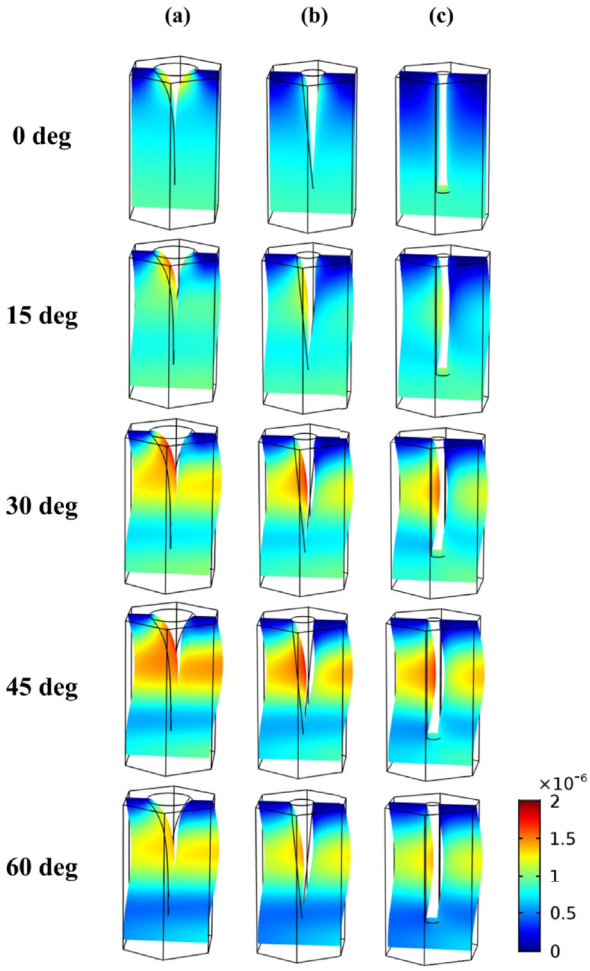

Fig. 21. Comparison of velocities in rubber domain at 3.2 kHz (unit:m/s) at different incidence angles for the: (a) horn hole; (b) conical hole; (c) cylindrical hole. The color denotes the value of the total velocity, and the deformations are magnified in the same value to denote the velocity size and direction.

oblique incidence excites global horizontal vibration modes bringing two sound absorption coefficient peak, so the three hole shapes have similar absorption curves. For local vibration dissipation, the volume of three kinds of hole shapes are not large enough to obviously change the global vibration. The holes mainly influence the part near themselves as shown in Figs. 13 and 14. Therefore, the fact that the horn hole has still a better sound absorption performance than the other two at relatively low frequencies in the oblique incidence situation, mainly depends on its local dissipation ability, as discussed in Section 3.3 for normal incidence.

4. Conclusions

A theoretical model has been developed to investigate the sound absorption performance of underwater anechoic layers containing periodically distributed axial holes for normal incidence, with focus placed on the influence of the topological shape of the hole. Three different types of axial holes are considered, the cylindrical hole, the conical, and the horn shaped one. FE simulations are performed to validate the proposed model, and excellent agreement is achieved. Furthermore, in consideration of the real working condition, a three-dimensional FE model for oblique incidence cases is developed to analyze the effects of hole shapes at different incidence angles on sound absorption performance.

For each type of hole in normal incidence situation, the absorption coefficient curve exhibits a crest at low frequency, a trough at middle frequency, and a relatively greater crest at high frequencies. The trough is attributed to small vibration displacement rather than vibration velocity. As to the crest at high frequency, radial vibration, which represents the propagation of transverse wave in the anechoic layer, plays a significant role. When the size of hole increases, the absorption coefficient curve shifts towards lower frequencies. When the size of hole is fixed, the horn hole has the best sound absorption performance at relatively low frequencies, due mainly to the great and fast axial and radial vibration at the horn mouth as well

as large and fast axial vibration in the middle and front portions of the anechoic layer. For oblique incidence situations, two new absorption peaks appear since the oblique incidence excites two horizontal modes, and the horn hole still has a better performance than others at relatively low frequencies. This research can be used to tailor the topological configuration of axially varying holes in high performance anechoic layers for specific underwater applications.

Acknowledgements

This work was supported by NSFC (11761131003, U1737107, 11772248 and 51528501), DFG (ZH15/32-1) and the Shaanxi Foundation for Selected Overseas Chinese (2017025).

Appendix A

Expressions of the twelve elements in the coefficient matrix of Eq. (11) are given by:

$$M_{11} = -k_{l,r}J_1(k_{l,r}r) \tag{A.1}$$

$$M_{12} = -k_{l,r}Y_1(k_{l,r}r) \tag{A.2}$$

$$M_{13} = -\mathrm{i}k_z k_{t,r}J_1(k_{t,r}r) \tag{A.3}$$

$$M_{14} = -\mathrm{i}k_z k_{t,r}Y_1(k_{t,r}r) \tag{A.4}$$

$$M_{21} = -\left[\lambda\left(k_{l,r}^2 + k_z^2\right) + 2\mu k_{l,r}^2\right]J_0(k_{l,r}r) + \frac{2\mu k_{l,r}}{r}J_1(k_{l,r}r) \tag{A.5}$$

$$M_{22} = -\left[\lambda\left(k_{l,r}^2 + k_z^2\right) + 2\mu k_{l,r}^2\right]Y_0(k_{l,r}r) + \frac{2\mu k_{l,r}}{r}Y_1(k_{l,r}r) \tag{A.6}$$

$$M_{23} = 2\mathrm{i}\mu k_{t,r}k_z\left[-k_{t,r}J_0(k_{t,r}r) + \frac{1}{r}J_1(k_{t,r}r)\right] \tag{A.7}$$

$$M_{24} = 2\mathrm{i}\mu k_{t,r}k_z\left[-k_{t,r}Y_0(k_{t,r}r) + \frac{1}{r}Y_1(k_{t,r}r)\right] \tag{A.8}$$

$$M_{31} = -2\mathrm{i}\mu k_{l,r}k_z J_1(k_{l,r}r) \tag{A.9}$$

$$M_{32} = -2\mathrm{i}\mu k_{l,r}k_z Y_1(k_{l,r}r) \tag{A.10}$$

$$M_{33} = \mu k_{t,r}\left(k_z^2 - k_{t,r}^2\right)J_1(k_{t,r}r) \tag{A.11}$$

$$M_{34} = \mu k_{t,r}\left(k_z^2 - k_{t,r}^2\right)Y_1(k_{t,r}r) \tag{A.12}$$

References

[1] F.G. Blake, Spherical wave propagation in solid media, J. Acoust. Soc. Am. 24 (1952) 211–214.
[2] R.M. White, Radiation impedance of a cylindrical bore in a solid, J. Acoust. Soc. Am. 29 (1957) 751–752.
[3] E. Meyer, K. Brendel, K. Tamm, Pulsation oscillations of cavities in rubber, J. Acoust. Soc. Am. 30 (1958) 1116–1124.
[4] G. Gaunaurd, One-dimensional model for acoustic absorption in a viscoelastic medium containing short cylindrical cavities, J. Acoust. Soc. Am. 62 (1977) 298–307.
[5] R. Lane, Absorption mechanisms for waterborne sound in Alberich anechoic layers, Ultrasonics 19 (1) (1981) 28–30.
[6] G. Gaunaurd, Comments on 'Absorption mechanisms for waterborne sound in Alberich anechoic layers', Ultrasonics 23 (2) (1985) 90–91.
[7] P.D. Jackins, G.C. Gaunaurd, Resonance reflection of acoustic waves by a perforated bilaminar rubber coating model, J. Acoust. Soc. Am. 73 (5) (1983) 1456–1463.
[8] H.C. Strifors, G.C. Gaunaurd, Selective reflectivity of viscoelastically coated plates in water, J. Acoust. Soc. Am. 88 (2) (1990) 901–910.
[9] P. Cervenka, P. Challande, A new efficient algorithm to compute the exact reflection and transmission factors for plane waves in layered absorbing media (liquids and solids), J. Acoust. Soc. Am. 89 (4) (1991) 1579–1589.
[10] P.R. Stepanishen, B. Strozeski, Reflection and transmission of acoustic wideband plane waves by layered viscoelastic media, J. Acoust. Soc. Am. 71 (1) (1982) 9–21.
[11] G. Liang, F. Pang, Acoustic characteristics of underwater composite materials at oblique incidence of sound wave, Noise Vib. Worldw. 44 (5) (2013) 12–17.
[12] W.L. Tang, S.P. He, J. Fan, Two-dimensional model for acoustic absorption of viscoelastic coating containing cylindrical holes, Acta Acustica 30 (4) (2005) 289–295.
[13] M. Tao, Simplified model for predicting acoustic performance of an underwater sound absorption coating, J. Vib. Contr. 20 (3) (2014) 339–354.
[14] A.C. HladkyHennion, J.N. Decarpigny, Analysis of the scattering of a plane acoustic wave by a doubly periodic structure using the finite element method: application to Alberich anechoic coatings, J. Acoust. Soc. Am. 90 (6) (1991) 3356–3367.

[15] V. Easwaran, M.L. Munjal, Analysis of reflection characteristics of a normal incidence plane wave on resonant sound absorbers: a finite element approach, J. Acoust. Soc. Am. 93 (3) (1993) 1308–1318.
[16] P. Langlet, A.C. HladkyHennion, J.N. Decarpigny, Analysis of the propagation of plane acoustic waves in passive periodic materials using the finite element method, J. Acoust. Soc. Am. 98 (5) (1995) 2792–2800.
[17] A.C. Hennion, R. Bossut, J.N. Decarpigny, C. Audoly, Analysis of the scattering of a plane acoustic wave by a periodic elastic structure using the finite element method: application to compliant tube gratings, J. Acoust. Soc. Am. 87 (5) (1990) 1861–1870.
[18] S.N. Panigrahi, C.S. Jog, M.L. Munjal, Multi-focus design of underwater noise control linings based on finite element analysis, Appl. Acoust. 69 (2008) 1141–1153.
[19] D.L. Peng, P. Hu, B.L. Zhu, The modified method of measuring the complex transmission coefficient of multilayer acoustical panel in impedance tube, Appl. Acoust. 69 (2008) 1240–1248.
[20] A.M. Baird, F.H. Kerr, D.J. Townend, Wave propagation in a viscoelastic medium containing fluid-filled microspheres, J. Acoust. Soc. Am. 105 (3) (1999) 1527–1538.
[21] H. Meng, J. Wen, H. Zhao, L. Lv, X. Wen, Analysis of absorption performances of anechoic layers with steel plate backing, J. Acoust. Soc. Am. 132 (1) (2012) 69–75.
[22] J. Wen, H. Zhao, L. Lv, B. Yuan, G. Wang, X. Wen, Effects of locally resonant modes on underwater sound absorption in viscoelastic materials, J. Acoust. Soc. Am. 130 (3) (2011) 1201–1208.
[23] M. Ghanbari, S. Hossainpour, G. Rezazadeh, Studying thin film damping in a micro-beam resonator based on non-classical theories, Acta Mech. Sin. 32 (3) (2016) 369–379.
[24] F. Xin, T.J. Lu, Acoustomechanical constitutive theory for soft materials, Acta Mech. Sin. 32 (5) (2016) 828–840.
[25] S.M. Ivansson, Sound absorption by viscoelastic coatings with periodically distributed cavities, J. Acoust. Soc. Am. 119 (6) (2006) 3558–3567.
[26] S.M. Ivansson, Numerical design of Alberich anechoic coatings with superellipsoidal cavities of mixed sizes, J. Acoust. Soc. Am. 124 (4) (2008) 1974–1984.
[27] S.M. Ivansson, Markov-chain Monte Carlo identification of favorable design choices with application to anechoic coatings, J. Acoust. Soc. Am. 135 (6) (2014) 3338–3351.
[28] C. Shang, J.Z. Zhang, Y.J. Wei, Absorption characteristics of anechoic coating embedding frustum-of-a-cone cavities, J. Ship Mech. 14 (12) (2010) 1425–1431.
[29] A.J. Hull, J.M. Maguire, Elastic response of an orthogonally reinforced plate, J. Sound Vib. 333 (8) (2014) 2327–2346.
[30] A.J. Hull, J.R. Welch, Elastic response of an acoustic coating on a rib-stiffened plate, J. Sound Vib. 329 (20) (2010) 4192–4211.
[31] F.X. Xin, Signal response of rib-stiffened plates covered by decoupling coating layers, J. Sound Vib. 348 (2015) 206–223.
[32] L. Jaouen, F.X. Becot, Acoustical characterization of perforated facings, J. Acoust. Soc. Am. 129 (3) (2011) 1400–1406.
[33] O. Dazel, F.X. Becot, L. Jaouen, Biot effects for sound absorbing double porosity materials, Acta Acust. Unit. Acust. 98 (4) (2012) 567–576.
[34] F. Chevillotte, C. Perrot, R. Panneton, Microstructure based model for sound absorption predictions of perforated closed-cell metallic foams, J. Acoust. Soc. Am. 128 (4) (2010) 1766–1776.
[35] C. Boutin, P. Royer, J.L. Auriault, Acoustic absorption of porous surfacing with dual porosity, Int. J. Solid Struct. 35 (34–35) (1998) 4709–4737.
[36] X. Olny, C. Boutin, Acoustic wave propagation in double porosity media, J. Acoust. Soc. Am. 114 (1) (2003) 73–89.
[37] F.C. Sgard, X. Olny, N. Atalla, F. Castel, On the use of perforations to improve the sound absorption of porous materials, Appl. Acoust. 66 (6) (2005) 625–651.
[38] J.D. Achenbach, Wave Propagation in Elastic Solids, North-Holland Publishing Company, Amsterdam, London, 1973.